A theoretical model of fuselage pressure levels due to fan tones radiated from the intake of an installed turbofan aero-engine

James Gaffney, Alan McAlpine, and Michael J. Kingan

Citation: The Journal of the Acoustical Society of America **143**, 3394 (2018); doi: 10.1121/1.5038263
View online: https://doi.org/10.1121/1.5038263
View Table of Contents: https://asa.scitation.org/toc/jas/143/6
Published by the Acoustical Society of America

A theoretical model of fuselage pressure levels due to fan tones radiated from the intake of an installed turbofan aero-engine

James Gaffney[a)] and Alan McAlpine
Institute of Sound and Vibration Research, University of Southampton, Southampton, SO17 1BJ, United Kingdom

Michael J. Kingan
Department of Mechanical Engineering, University of Auckland, Auckland, New Zealand

(Received 28 September 2017; revised 30 April 2018; accepted 2 May 2018; published online 7 June 2018)

An existing theoretical model to predict the pressure levels on an aircraft's fuselage is improved by incorporating a more physically realistic method to predict fan tone radiation from the intake of an installed turbofan aero-engine. Such a model can be used as part of a method to assess cabin noise. Fan tone radiation from a turbofan intake is modelled using the exact solution for the radiated pressure from a spinning mode exiting a semi-infinite cylindrical duct immersed in a uniform flow. This approach for a spinning duct mode incorporates scattering/diffraction by the intake lip, enabling predictions of the radiated pressure valid in both the forward and aft directions. The aircraft's fuselage is represented by an infinitely long, rigid cylinder. There is uniform flow aligned with the cylinder, except close to the cylinder's surface where there is a constant-thickness boundary layer. In addition to single mode calculations it is shown how the model may be used to rapidly calculate a multi-mode incoherent radiation from the engine intake. Illustrative results are presented which demonstrate the relative importance of boundary-layer shielding both upstream and downstream of the source, as well as examples of the fuselage pressure levels due to a multi-mode tonal source at high Helmholtz number. https://doi.org/10.1121/1.5038263

[DDE] Pages: 3394–3405

I. INTRODUCTION

In modern civil aircraft, turbofan jet engines are the dominant noise source during take-off and cruise. Successive legislative and certification requirements have set stringent targets for reductions in noise emissions from civil aircraft. Reducing the impact of aircraft noise requires reliable and fast noise prediction tools which can be used for engineering optimisation studies during the development of new quieter engines. Owing to the complexity of the turbomachinery, it is routine to separately predict the sound radiation from individual sources (such as the fan, turbine and jet). Normally the sound radiation is modelled in the free field but, in reality, sound radiation can be affected by the airframe.

Installation acoustics for turbofan jet engines refers to the study of how the radiated noise is affected when an engine is installed on an airframe. Of particular relevance is the pressure levels on the aircraft's fuselage since the sound transmitted through the fuselage will directly affect the cabin noise levels. Fan tones radiating from an engine intake duct, particularly "buzz-saw" tones which are produced when the fan tip speed is supersonic, can radiate at very high pressure amplitudes. Predicting the pressure levels on the fuselage surface is required in order to assess what acoustic treatments must be applied in order to achieve an acceptable cabin noise level.

In this theoretical model, the source or incident field represents a fan tone radiated from a turbofan intake. Adjacent to the intake, an infinitely long, rigid cylinder represents a cylindrical fuselage. The scattering method can be used to determine the pressure field everywhere, albeit in this work attention is focussed on the pressure levels on the cylinder.

The solution of the scattered field due to an acoustic monopole located adjacent to an infinite, rigid cylinder in a stationary fluid is given in the text by Bowman *et al.*[1] (Chap. 2, Sec. 2.5.2, pp. 126–127). By solving the convected wave equation rather than the wave equation, the solution for the scattered field in the presence of a uniform axial flow aligned with the cylinder axis can also be derived. However, for the purpose of modelling sound propagation from the engine intake to the fuselage surface, the effect of refraction within the fuselage boundary layer must be taken into account. Sound propagating upstream is refracted away from the surface of the fuselage by the boundary layer, which is referred to as "shielding." Early examples of this include McAninch[2] and Hanson[3] with studies of a monopole over a flat plate with a boundary layer. Following this, a significant advance was presented by Hanson and Magliozzi[4] who developed an installation acoustics model of a propeller-type source located adjacent to an infinite, rigid cylinder in the presence of an axial mean flow including a boundary layer on the cylinder. Later, Lu[5] added a temperature gradient to the boundary layer, although this was found to be inconsequential on the shielding. More recently, Belyaev[6] and Brouwer[7]

[a)] Electronic mail: jamesapgaffney@gmail.com

0001-4966/2018/143(6)/3394/12

studied the effects of installed open-rotor engines. Generally, all these papers found that significant shielding can be caused by the boundary layer upstream of the source, thereby reducing the pressure levels on the surface of the fuselage, but the shielding and effect on the pressure levels caused by the boundary layer is minimal downstream of the source.

There is far less research on fan tone sources radiated from turbofan aero-engines, and the resulting fuselage pressure levels. Siefert and Delfs[8] and Dierke *et al.*[9] have employed Computational Aero-Acoustics (CAA) methods to predict the scattering and refraction by the fuselage of a spinning mode radiated from a turbofan intake duct. The computational method was also able to examine the effect of spectral broadening.

The current article is a continuation of theoretical work by the authors,[10,11] on prediction of the fuselage pressure levels due to intake fan tone radiation. In McAlpine *et al.*,[10] the pressure levels on a cylindrical fuselage forward of the intake duct were simulated using a theoretical solution based on an incident field given by a distributed "disk" acoustic source located adjacent to an infinite, rigid cylinder. The disk source derivation was based on the Rayleigh integral adopted by Tyler and Sofrin.[12] In this earlier work, the mean flow was taken to be a uniform axial flow aligned with the axis of the cylinder. Subsequently, this theoretical solution was extended by Gaffney *et al.*[11] to include the fuselage boundary layer. This requires the numerical solution of the Pridmore-Brown equation in the boundary-layer region which is matched to the solution for the convected wave equation (uniform flow) at the edge of the boundary layer.

The key advancement in the current article is to use the full Wiener–Hopf solution for a spinning mode exiting a cylindrical duct, instead of the disk source, to specify the incident field. The Wiener–Hopf solution gives the pressure radiated into a free field. It is shown how to combine this solution with the cylindrical fuselage scattering method. Combining these two existing methods gives a theoretical installation acoustics model for intake fan noise, with an adjacent cylindrical fuselage in the near field, and inclusion of the fuselage boundary-layer which can shield the forward radiated fan noise. Thus, new results in this article focus on the predicted shielding effect of the boundary layer for intake fan tone radiation. Additionally, it is shown how to use the model to rapidly calculate a multi-mode incoherent source, as opposed to calculations for the radiation of a single mode.

The benefit of using the incident field given by the Wiener–Hopf solution for a spinning mode incorporates scattering/diffraction by the intake lip, and accounts for reflection of sound at the exit plane of the intake. Thus, it provides a more realistic incident field compared to the disk source model which does not account for the effects of the intake duct. The other key benefit of using the incident field given by the Wiener–Hopf solution for a spinning mode is that predictions will be more realistic near the source plane ($\theta = 90°$), and can be extended to downstream ($\theta > 90°$). This is not possible with the disk source model whose predictions only will be realistic up to a maximum polar angle, say $\theta_{\max}$, where $\theta_{\max} < 90°$.

The overall situation is shown sketched in Fig. 1 which illustrates for wing-mounted engines the intake fan noise installation acoustics model. Both forward and aft radiated fan noise from modern turbofan aero-engines are significant contributors to the overall noise. Modelling radiation of fan noise

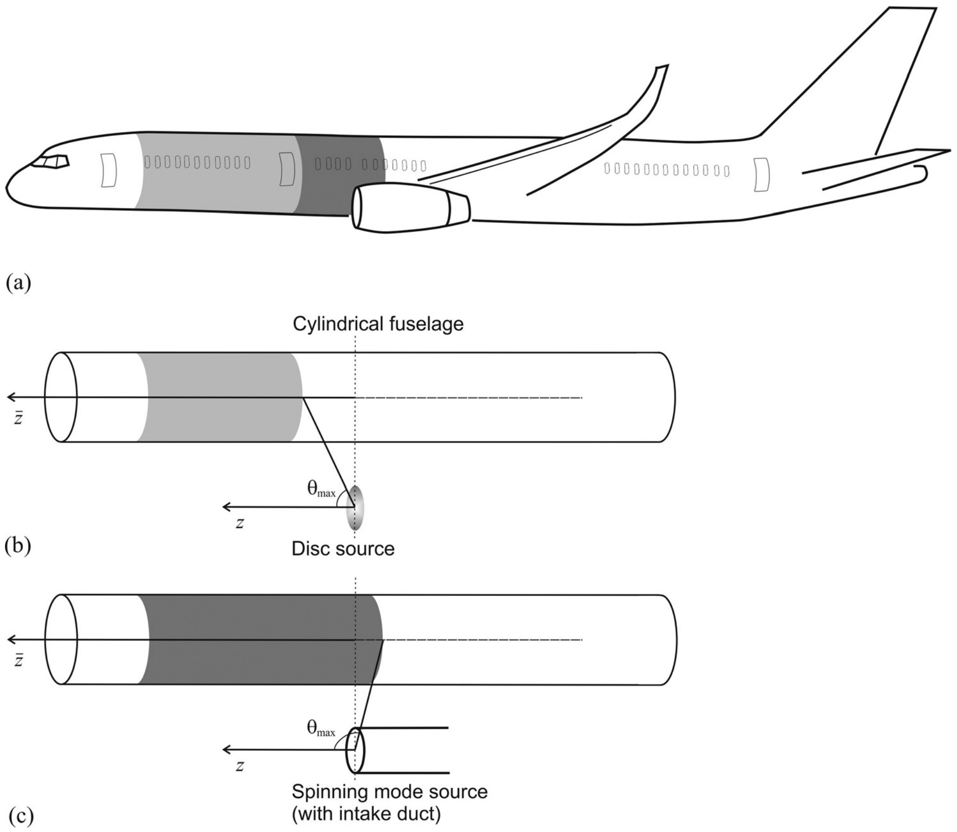

FIG. 1. Canonical problem for intake fan tone radiation from an installed turbofan aero-engine. (a) Sketch of an installed turbofan aero-engine mounted below the wings. (b) Incident field = disk source. (c) Incident field = Spinning mode. Polar angle $\theta_{\max}$ indicates, along with the shaded regions, roughly where predictions of the fuselage pressure levels are valid.

from the bypass duct increases the complexity of the prediction method because it is necessary to model the noise propagating through the exhaust jet shear layers. Additionally, there are other significant contributors to the aft radiated noise such as core, turbine and jet noise sources, and for engines mounted under the wings, the propagation and radiation of exhaust noise will be affected by the wings.

Consequently, it is assumed that noise radiated from the intake which is incident on the fuselage is the dominant source forward of the aircraft wings, but it is expected that downstream of the wings, the exhaust noise sources would be required for realistic predictions of the fuselage pressure levels. Thus, although the Wiener–Hopf solution is valid at all polar angles, i.e., both upstream and downstream, it is emphasised that further downstream the fuselage pressure levels will be dominated by exhaust noise sources. Without predicting the levels of other (exhaust) noise sources, the maximum polar angle at which the intake fan noise radiation is the dominant source cannot be precisely quantified. As shown in Fig. 1, the polar range over which the intake fan noise method should be reasonably applied, using either the disk source or the spinning mode source to specify the incident field, is illustrated. This illustrates the significant increase in the area of the fuselage where predictions of the pressure levels can be applied using the Wiener–Hopf solution for a spinning mode, compared to utilising the disk source for the incident field. In this work, the focus is intake fan tone noise, predominantly "buzz-saw" tones, incident on this portion of the fuselage forward of the wings.

II. THEORY

A sketch of the problem set-up is shown in Fig. 2. The Cartesian reference frame for the intake is (x, y, z), or equivalently in cylindrical polar coordinates (r, ϕ, z), where the centre of the intake is aligned with the z-axis, and the duct termination is at $z = 0$. The Cartesian reference frame for the fuselage is $(\bar{x}, \bar{y}, \bar{z})$, or equivalently in cylindrical polar coordinates $(\bar{r}, \bar{\phi}, \bar{z})$. There is a subsonic uniform mean flow, Mach number M_∞, directed in the negative $\bar{z}$-direction. Also there is a fuselage boundary layer with constant thickness δ.

In the following analysis, all values are dimensionless: the reference length scale is equal to the fuselage radius a_0; the reference velocity is the speed of sound c_0; the reference density is ρ_0, and the pressure is scaled by $\rho_0 c_0^2$.

The principal difference between the theory in this article compared to the theory presented in Gaffney *et al.*[11] is the method to calculate the incident field. In the previous article,[11] fan tone radiation from an intake is represented by a disk source model. In the current article, fan tone radiation is calculated using the Wiener–Hopf solution for a spinning mode radiated from a cylindrical intake duct. This solution was given by Homicz and Lordi in 1975,[13] albeit we have used a more recent formulation taken from Gabard and Astley[14] which itself was based on the formulation by Munt.[16] Subsequently the procedure to calculate the scattered field, and to construct the total field, is the same as detailed in Gaffney *et al.*[11] (Sec. II). Accordingly, in this article, only the theory for the incident field is covered in detail, and for brevity, only brief details are given about the procedure to calculate the fuselage scattering including the boundary-layer refraction.

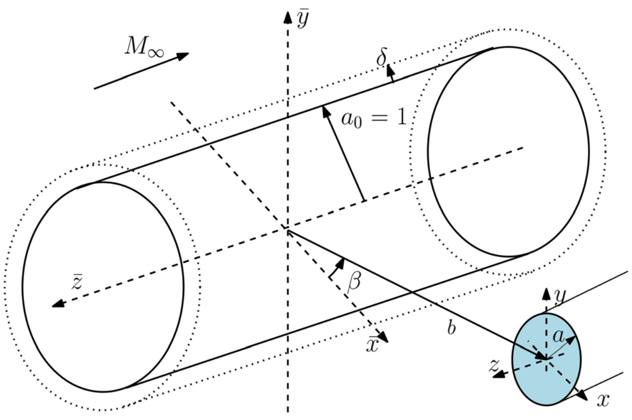

FIG. 2. (Color online) Sketch of the cylindrical fuselage (radius a_0) and the circular intake duct (radius a). The centreline of the cylinder is aligned with the $\bar{z}$-axis, the intake duct is aligned with the z-axis, and the duct termination is located in the plane $z = \bar{z} = 0$. The transverse distance between the centre of the intake duct and the centre of the cylinder is b. Also shown is the edge of the fuselage boundary-layer (thickness δ).

A. In-duct sound field

The intake is modelled by a cylindrical duct with a rigid, impervious and infinitesimal wall. The duct has radius a and is semi-infinite, $-\infty < z < 0$. The flow velocity inside the duct is the same as the flow outside the duct, i.e., Mach number M_∞ directed in the negative z-direction. It is also noted that the ambient density ρ_0, and speed of sound c_0 are uniform everywhere.

The in-duct acoustic pressure field is defined in terms of spinning modes.[12] Each mode is defined by its integer azimuthal order l and radial order q. Time-harmonic solutions are expressed by $p_{lq} = \hat{p}_{lq}(r,z)\,\exp\{\mathrm{i}(\omega_0 t - l\phi)\}$ and $u_{z,lq} = \hat{u}_{z,lq}(r,z)\,\exp\{\mathrm{i}(\omega_0 t - l\phi)\}$ for the acoustic pressure and axial particle velocity, respectively, noting that the values are normalised such that $k_0 = \omega_0$. These are found by solving the convected Helmholtz equation, which gives

$$\hat{p}_{lq}(r,z) = P_{lq}\mathrm{J}_l(\kappa_{lq} r)\mathrm{e}^{-\mathrm{i}k_{z\,lq} z}, \tag{1}$$

$$\hat{u}_{z,lq}(r,z) = \xi_{lq} P_{lq}\mathrm{J}_l(\kappa_{lq} r)\mathrm{e}^{-\mathrm{i}k_{z\,lq} z}, \tag{2}$$

where P_{lq} is the modal amplitude, $\mathrm{J}_l(\cdot)$ denotes the Bessel function of the first kind of order l, and $\kappa_{lq}, k_{z,lq}$ denote the radial and axial wavenumber of mode (l, q), respectively. The rigid boundary condition on the duct wall gives the radial wavenumber which corresponds to the lth turning point of the Bessel function. The acoustic pressure and particle velocity are linked via the factor

$$\xi_{lq} = \frac{k_{z,lq}}{k_0 + k_{z,lq} M_\infty}, \tag{3}$$

and the dispersion relationship (valid for the in-duct field) is given by

$$k_{z,lq}^2 + \kappa_{lq}^2 = (k_0 + k_{z,lq} M_\infty)^2. \tag{4}$$

The modal amplitude can be related to the modal power W_{lq} via

$$|P_{lq}| = \sqrt{\frac{2W_{lq}}{\pi\left[a^2 - \left(l/\kappa_{lq}\right)^2\right]\mathrm{J}_l^2(\kappa_{lq}a)\left[\left(1+M_\infty^2\right)\mathrm{Re}\left\{\xi_{lq}\right\} - M_\infty\left(1+|\xi_{lq}|^2\right)\right]}}. \tag{5}$$

This relation will be used to specify the amplitude of each mode to form an incoherent, equal-power-per-mode source for which illustrative examples are provided in Sec. IV.

B. Incident field

The Wiener–Hopf formulation by Gabard and Astley[14] for a spinning mode radiated from a cylindrical duct is used to determine the incident field. The key parts of the derivation are outlined in this section. Full details and how to implement the solution are given in Ref. 14. Differences between this and the formulation by Gabard and Astley is the convention for time-harmonic quantities and the choice of reference length scale.[15] The complex frequency is defined as $\omega = |\omega|\mathrm{e}^{j\epsilon}$ with $-\pi/2 \le \epsilon \le 0$, this is the complex conjugate of Ref. 14. Also, Gabard and Astley derived the solution based on a velocity potential formulation, whereas in this article the key steps in the analysis are formulated in terms of the pressure.

The problem is defined such that the incident field $\hat{p}_i$ for mode (l, q) is given by a summation of the (in-duct) spinning mode, given by Eq. (1), and a diffracted field $\hat{p}_d$, such that

$$\hat{p}_i = \begin{cases} \hat{p}_{lq} + \hat{p}_d, & r < a, \\ \hat{p}_d, & r > a. \end{cases} \tag{6}$$

Since the walls of the duct have infinitesimal thickness, conditions are specified taking the limits as $r \to a^-$ and $r \to a^+$, where the superscript $-$ denotes approaching $r = a$ from $r < a$, and the superscript $+$ denotes approaching $r = a$ from $r > a$. In the region $z < 0$, this corresponds to taking the limit inside or outside the duct. Therefore, on the rigid duct wall the radial particle velocity is zero. This is equivalent to zero pressure gradient, i.e.,

$$\frac{\partial \hat{p}_i(a^-, z)}{\partial r} = \frac{\partial \hat{p}_i(a^+, z)}{\partial r} = 0, \quad z < 0. \tag{7}$$

Forward of the duct, there is pressure continuity, i.e.,

$$\hat{p}_i(a^-, z) = \hat{p}_i(a^+, z), \quad z \ge 0, \tag{8}$$

$$\Rightarrow \ \hat{p}_{lq}(a^-, z) + \hat{p}_d(a^-, z) = \hat{p}_d(a^+, z), \quad z \ge 0. \tag{9}$$

Therefore, the diffracted field must be discontinuous at $r = a$ for $z \ge 0$. The pressure jump in the diffracted field is

$$\Delta\hat{p}_d = \hat{p}_d(a^+, z) - \hat{p}_d(a^-, z) = \hat{p}_{lq}(a^-, z), \quad z \ge 0. \tag{10}$$

The solution is found by taking a Fourier transform in the axial position z, however, the Fourier transform is split into two half-range transforms to take account of the different boundary conditions on $r = a$ for $z < 0$ and $z \ge 0$, i.e.,

$$\tilde{p}_{d-}(r, \bar{k}_z) = \int_{-\infty}^{0} \hat{p}_d(r, z)\, \mathrm{e}^{\mathrm{i}k_0\bar{k}_z z}\, \mathrm{d}z, \tag{11a}$$

$$\tilde{p}_{d+}(r, \bar{k}_z) = \int_{0}^{\infty} \hat{p}_d(r, z)\, \mathrm{e}^{\mathrm{i}k_0\bar{k}_z z}\, \mathrm{d}z, \tag{11b}$$

where $\bar{k}_z = k_z/k_0$. The full transform is

$$\tilde{p}_d = \tilde{p}_{d-} + \tilde{p}_{d+}. \tag{12}$$

Following Gabard and Astley,[14] it can be shown that $\tilde{p}_{d\pm}$ are regular in the half-planes $R_\pm$ where $R_\pm$: $\mp\mathrm{Im}(\bar{k}_z - \bar{k}_z^\pm) < \mp\tan(\epsilon)\mathrm{Re}(\bar{k}_z - \bar{k}_z^\pm)$.

Upon Fourier transformations, the convected Helmholtz equation reduces to Bessel's differential equation, and the solutions are chosen as

$$\tilde{p}_d(r, \bar{k}_z) = \begin{cases} A(\bar{k}_z)\,\mathrm{H}_l^{(2)}(k_0\Gamma_0 r), & r > a, \\ B(\bar{k}_z)\,\mathrm{J}_l(k_0\Gamma_0 r), & r < a. \end{cases} \tag{13}$$

Note that $\mathrm{H}_l^{(2)}(\cdot)$ is the Hankel function of the second kind of order l. This solution is selected for $r > a$ because it satisfies the appropriate radiation condition as $r \to \infty$ (outward propagating wave). The other solution with $\mathrm{J}_l(\cdot)$ is selected for $r < a$ because it satisfies the finiteness condition at $r = 0$. The amplitude coefficients $A(\bar{k}_z)$ and $B(\bar{k}_z)$ are to be found in the following analysis. The free-field radial wavenumber, Γ_0, is linked via the dispersion relationship

$$\bar{k}_z^2 + \Gamma_0^2 = (1 + \bar{k}_z M_\infty)^2. \tag{14}$$

This can be written as $\Gamma_0 = \Gamma_0^+\Gamma_0^-$, where

$$\begin{aligned} \Gamma_0^+ &= \left[1 + (M_\infty - 1)\bar{k}_z\right]^{1/2}, \\ \Gamma_0^- &= \left[1 + (M_\infty + 1)\bar{k}_z\right]^{1/2}, \end{aligned} \tag{15}$$

where $\Gamma_0^\pm$ have zeros at

$$\bar{k}_z^- = -\frac{1}{1 + M_\infty} \quad \text{and} \quad \bar{k}_z^+ = \frac{1}{1 - M_\infty}. \tag{16}$$

Define the transform of the radial particle displacement $\hat{\varepsilon}_r$ on $r = a$ by W. This reduces to the half-range transform

$$W_+(\bar{k}_z) = \int_0^\infty \hat{\varepsilon}_r(a, z)\, \mathrm{e}^{\mathrm{i}k_0\bar{k}_z z}\, \mathrm{d}z, \tag{17}$$

since the radial particle velocity is zero on the rigid duct, hence $W_- = 0$.

Then taking the transform of the radial component of the linearised momentum equation, and substituting Eqs. (13) and (17), gives

$$\begin{aligned}(1+\bar{k}_z M_\infty)^2 W_+ &= A(\bar{k}_z)\Gamma_0 \mathrm{H}_l^{(2)\prime}(k_0\Gamma_0 a)\\ &= B(\bar{k}_z)\,\Gamma_0 \mathrm{J}_l^{\prime}(k_0\Gamma_0 a).\end{aligned} \tag{18}$$

The objective is to find $A(\bar{k}_z)$ and $B(\bar{k}_z)$ by deriving an expression for W_+. The transform of the pressure jump of the diffracted field [Eq. (10)] is

$$G(\bar{k}_z) = \int_{-\infty}^{\infty} \Delta\hat{p}_d\, \mathrm{e}^{\mathrm{i}k_0\bar{k}_z z}\,\mathrm{d}z, \tag{19}$$

$$= \int_{-\infty}^{\infty} \left[\hat{p}_d(a^+,z) - \hat{p}_d(a^-,z)\right] \mathrm{e}^{\mathrm{i}k_0\bar{k}_z z}\,\mathrm{d}z, \tag{20}$$

which, from Eq. (13), leads to

$$G(\bar{k}_z) = A(\bar{k}_z)\,\mathrm{H}_l^{(2)}(k_0\Gamma_0 a) - B(\bar{k}_z)\,\mathrm{J}_l(k_0\Gamma_0 a). \tag{21}$$

However, since the pressure is continuous on $r=a$ for $z>0$, combining Eqs. (1), (10), and (20), the positive half-range transform of G can be evaluated analytically,

$$\begin{aligned}G_+(\bar{k}_z) &= P_{lq}\int_0^{\infty} \mathrm{J}_l(\kappa_{lq}a)\,\mathrm{e}^{-\mathrm{i}k_0\bar{k}_{z,lq}z}\,\mathrm{e}^{\mathrm{i}k_0\bar{k}_z z}\,\mathrm{d}z\\ &= \mathrm{i}P_{lq}\frac{\mathrm{J}_l(\kappa_{lq}a)}{k_0\bar{k}_{z,lq} - k_0\bar{k}_z},\end{aligned} \tag{22}$$

where $\bar{k}_{z,lq} = k_{z,lq}/k_0$. Next, substituting for $A(\bar{k}_z)$ and $B(\bar{k}_z)$ from Eq. (18)

$$G(\bar{k}_z) = G_-(\bar{k}_z) + G_+(\bar{k}_z) = \frac{W_+}{\Gamma_0^2}K, \tag{23}$$

where the kernel K is

$$K(k_z\bar{k}_z) = (1+\bar{k}_z M_\infty)^2\Gamma_0\left(\frac{\mathrm{H}_l^{(2)}(k_0\Gamma_0 a)}{\mathrm{H}_l^{(2)\prime}(k_0\Gamma_0 a)} - \frac{\mathrm{J}_l(k_0\Gamma_0 a)}{\mathrm{J}_l^{\prime}(k_0\Gamma_0 a)}\right). \tag{24}$$

The functions will be factorised into analytic and non-analytic functions. Thus, factorise K such that

$$K = \frac{K_+}{K_-}(\bar{k}_z - \bar{k}_{z0})^2, \tag{25}$$

where K_+ and K_- are regular, and $\bar{k}_{z0} = -\bar{k}_0/M_\infty$. When substituted into Eq. (23) this gives

$$\begin{aligned}&G_-(\bar{k}_z)K_-(\bar{k}_z)\Gamma_0^{-2} + G_+(\bar{k}_z)K_-(\bar{k}_z)\Gamma_0^{-2}\\ &\quad= \frac{W_+(\bar{k}_z)}{\Gamma_0^{+2}}\,K_+(\bar{k}_z)(\bar{k}_z - k_{z0})^2.\end{aligned} \tag{26}$$

Equation (26) is modified to ensure that the left hand side is R_-,

$$\begin{aligned}&G_-(\bar{k}_z)K_-(\bar{k}_z)\Gamma_0^{-2}(\bar{k}_z) + G_+(\bar{k}_z)K_-(\bar{k}_z)\Gamma_0^{-2}(\bar{k}_z)\\ &\qquad - \Gamma_0^{-2}(\bar{k}_{z,lq})K_-(\bar{k}_{z,lq})G_+(\bar{k}_z)\\ &\quad= \frac{W_+(\bar{k}_z)}{\Gamma_0^{+2}(\bar{k}_z)}\,K_+(\bar{k}_z)(\bar{k}_z - k_{z0})^2\\ &\qquad - \Gamma_0^{-2}(\bar{k}_{z,lq})K_-(\bar{k}_{z,lq})G_+(\bar{k}_z).\end{aligned} \tag{27}$$

Then, using Liouville's theorem both sides of Eq. (27) are equal to a constant, say E. Let $E(\bar{k}_{z0}) = -\Gamma_0^{-2}(\bar{k}_{z,lq})$ $K_-(\bar{k}_{z,lq})G_+(\bar{k}_{z0})$ so that W_+ is given by

$$\begin{aligned}W_+(\bar{k}_z) &= -\Gamma_0^{-2}(\bar{k}_{z,lq})\Gamma_0^{+2}(\bar{k}_z)\frac{K_-(\bar{k}_{z,lq})}{K_+(\bar{k}_z)(\bar{k}_z - \bar{k}_{z0})^2}\\ &\qquad\times\left[G_+(\bar{k}_{z0}) - G_+(\bar{k}_z)\right].\end{aligned} \tag{28}$$

Using the method in Gabard and Astley[14] (Appendix A), the functions K_- and K_+ can be evaluated. This gives

$$A(\bar{k}_z) = (1+\bar{k}_z M_\infty)^2\frac{W_+(\bar{k}_z)}{\Gamma_0\mathrm{H}_l^{(2)\prime}(k_0\Gamma_0 a)}, \tag{29a}$$

$$B(\bar{k}_z) = (1+\bar{k}_z M_\infty)^2\frac{W_+(\bar{k}_z)}{\Gamma_0\mathrm{J}_l^{\prime}(k_0\Gamma_0 a)}. \tag{29b}$$

Thus, combining Eqs. (13) and (29), the transformed incident pressure field is given by

$$\tilde{p}_d(r,\bar{k}_z) = (1+\bar{k}_z M_\infty)^2\frac{W_+}{\Gamma_0}\begin{cases}\dfrac{\mathrm{H}_l^{(2)}(k_0\Gamma_0 r)}{\mathrm{H}_l^{(2)\prime}(k_0\Gamma_0 a)}, & r>a,\\[2ex] \dfrac{\mathrm{J}_l(k_0\Gamma_0 r)}{\mathrm{J}_l^{\prime}(k_0\Gamma_0 a)}, & r<a.\end{cases} \tag{30}$$

Only the incident field for $r>a$ will be required for the cylinder scattering problem. Thus, the required field, for a spinning mode of amplitude P_{lq}, is expressed as

$$\tilde{p}_i\,(r,\bar{k}_z) = \tilde{p}_d\,(r,\bar{k}_z) = \tilde{\zeta}_{lq}(\bar{k}_z)\,\mathrm{H}_l^{(2)}(k_0\Gamma_0 r), \tag{31}$$

where

$$\tilde{\zeta}_{lq}(\bar{k}_z) = \frac{(1+\bar{k}_z M_\infty)^2 W_+}{\Gamma_0\mathrm{H}_l^{(2)\prime}(k_0\Gamma_0 a)}. \tag{32}$$

Then on taking the inverse Fourier transform, the incident field is given by

$$\hat{p}_i(r,\phi,z) = \frac{1}{2\pi}\int_{-\infty}^{\infty}\tilde{\zeta}_{lq}(\bar{k}_z)\,\mathrm{H}_l^{(2)}(k_0\Gamma_0 r)\,\mathrm{e}^{-\mathrm{i}k_0\bar{k}_z z}\,\mathrm{d}\bar{k}_z\,\mathrm{e}^{-\mathrm{i}l\phi}. \tag{33}$$

The integration contour is deformed from the real axis by analytic continuation such that the functions are regular. This means avoiding poles in K caused by the acoustic modes in the duct. The location of the poles are the complex conjugate of those found in Ref. 14.

The key result is the complex amplitude of the incident field $\tilde{\zeta}_{lq}$ [Eq. (32)], which depends on W_+ [Eq. (28)]. This is adapted from Gabard and Astley[14] [Eq. (3.22)]. It is emphasised that this is not a new result, since it gives the pressure field for a spinning duct mode radiated from a cylindrical duct, but Eq. (31) is formulated so that the incident field can be combined with the scattered field to determine the total field resulting from fuselage scattering.

C. Fuselage scattering including boundary-layer refraction

Having determined the incident pressure for a spinning mode radiated from a cylindrical duct into a free field, the objective is to determine the total field in the presence of a cylindrical fuselage located adjacent to the intake duct. The effect of refraction as the sound propagates through the fuselage boundary layer is included in the modelling.

The basic procedure now follows the method outlined in McAlpine *et al.*,[10] with the method to include the boundary layer outlined in Gaffney *et al.*[11] Graf's addition theorem[10] [Eq. (25)] is used to transform the incident field to the cylindrical polar coordinate system $(\bar{r}, \bar{\phi}, \bar{z})$ centred on the cylindrical fuselage. This transforms Eq. (33) to

$$\hat{p}_i(\bar{r},\bar{\phi},\bar{z}) = \frac{1}{(2\pi)^2}\sum_{n=-\infty}^{\infty}\left(\int_{-\infty}^{\infty}\tilde{p}_{i,n}(\bar{r},\bar{k}_z)\,\mathrm{e}^{-\mathrm{i}k_0\bar{k}_z\bar{z}}\,\mathrm{d}\bar{k}_z\right)\mathrm{e}^{-\mathrm{i}n\bar{\phi}}, \tag{34}$$

where

$$\tilde{p}_{i,n}(\bar{r},\bar{k}_z) = 2\pi\tilde{\zeta}_{lq}(\bar{k}_z)(-1)^{(l+n)}\mathrm{e}^{-\mathrm{i}(l-n)\beta} \times \mathrm{H}^{(2)}_{l-n}(k_0\Gamma_0 b)\,\mathrm{J}_n(k_0\Gamma_0\bar{r}). \tag{35}$$

It is important to note that $\tilde{\zeta}_{lq}(\bar{k}_z)$ is not affected by the transformation of coordinates.

The incident field is now defined. The method to incorporate fuselage scattering including boundary-layer shielding refraction now follows the same procedure outlined in Gaffney *et al.*[11] (Sec. II B).

An inviscid compressible isentropic perfect gas flow is assumed. The mean flow is assumed to be axisymmetric, parallel and directed in the negative axial direction, with constant mean density and sound speed profiles inside the boundary layer. The velocity profile M_z is given by

$$M_z = \begin{cases} M(\bar{r}), & 1 < \bar{r} \leq 1+\delta, \\ M_\infty, & 1+\delta < \bar{r}, \end{cases} \tag{36}$$

where δ is the non-dimensional thickness of the boundary-layer, and $M(\bar{r})$ is the boundary-layer Mach number profile. Note that the non-dimensional radius of the fuselage is unity.

Outside the boundary layer, where there is uniform flow, the acoustic pressure field is found by solving the convected Helmholtz equation. In this region, each azimuthal component of the total pressure field can be expressed in the form

$$\tilde{p}_n(\bar{r},\bar{k}_z) = \tilde{\eta}_n(\bar{k}_z)\,\mathrm{J}_n(k_0\Gamma_0\bar{r}) + \tilde{\gamma}_n(\bar{k}_z)\,\mathrm{H}^{(2)}_n(k_0\Gamma_0\bar{r}), \tag{37}$$

where $\tilde{\eta}_n(\bar{k}_z)$ and $\tilde{\gamma}_n(\bar{k}_z)$ are amplitude coefficients of the incident and cylindrical scattered waves, respectively.

Inside the boundary-layer region, the acoustic pressure field will satisfy the Pridmore-Brown equation,

$$\left[\frac{\mathrm{d}^2}{\mathrm{d}\bar{r}^2} + \left(\frac{1}{\bar{r}} - \frac{2\bar{k}_z M'}{1+\bar{k}_z M}\right)\frac{\mathrm{d}}{\mathrm{d}\bar{r}} + \left(k_0^2\Gamma_0^2 - \frac{n^2}{\bar{r}^2}\right)\right]\tilde{p}_{bl_n} = 0, \tag{38}$$

where $M' = \mathrm{d}M/\mathrm{d}\bar{r}$.

There is no known analytical solution to the Pridmore-Brown equation, therefore a standard Runge–Kutta ordinary differential solver is utilised. Accordingly, the transformed pressure in the boundary layer is normalised, i.e.,

$$\tilde{p}_{bl,n}(\bar{r},\bar{k}_z) = \tilde{\alpha}_n(\bar{k}_z)\tilde{f}_{bl,n}(\bar{r},\bar{k}_z), \tag{39}$$

where $\tilde{f}_{bl,n}$ is the normalised pressure, which is scaled by $\tilde{\alpha}_n(\bar{k}_z)$. On the surface of the rigid cylinder ($\bar{r} = a_0 = 1$), the boundary conditions are

$$\tilde{p}_{bl,n}(1,\bar{k}_z) = \tilde{\alpha}_n(\bar{k}_z) \quad \text{and} \quad \tilde{p}'_{bl,n}(1,\bar{k}_z) = 0. \tag{40}$$

The value of $\tilde{\alpha}_n$ must be proportional to the incoming wave. In order to formulate $\tilde{\alpha}_n$ in terms of the incident wave amplitude, matching conditions are applied at the edge of the boundary layer ($\bar{r} = 1+\delta$) to enforce continuity of pressure and the pressure gradient. The pressure in the boundary layer is scaled to match the amplitude of the incoming wave, i.e.,

$$\tilde{\alpha}_n(\bar{k}_z) = \tilde{\Lambda}_n(\bar{k}_z)\tilde{\eta}_n(\bar{k}_z), \tag{41}$$

where

$$\tilde{\Lambda}_n(\bar{k}_z) = -\frac{2\mathrm{i}}{\pi[1+\delta]}\,\frac{1}{\tilde{f}_{bl_n}\Big|_{1+\delta}k_0\Gamma_0\mathrm{H}^{(2)\prime}_n(k_0\Gamma_0[1+\delta]) - \tilde{f}'_{bl_n}\Big|_{1+\delta}\mathrm{H}^{(2)}_n(k_0\Gamma_0[1+\delta])}, \tag{42}$$

and

$$\tilde{\eta}_n(\bar{k}_z) = 2\pi\tilde{\zeta}_{lq}(\bar{k}_z)(-1)^{(l+n)}\mathrm{e}^{-\mathrm{i}(l-n)\beta}\mathrm{H}^{(2)}_{l-n}(k_0\Gamma_0 b). \tag{43}$$

It is noted that $\tilde{\Lambda}_n(\bar{k}_z)$ is a function that depends on the boundary-layer profile, but it does not depend on the spinning mode order (l, q), whereas the amplitude coefficient $\tilde{\eta}_n(\bar{k}_z)$ depends on the spinning mode (l, q), but it does not depend on the boundary-layer profile.

Finally, on the surface of the cylinder, the pressure can be calculated via

$$\hat{p}_t\left(a_0,\bar{\phi},\bar{z}\right) = \frac{1}{(2\pi)^2}\sum_{n=-\infty}^{\infty}\left\{\int_{-\infty}^{\infty}\tilde{\alpha}_n(\bar{k}_z)\,\mathrm{e}^{-\mathrm{i}k_0\bar{k}_z\bar{z}}\,\mathrm{d}\bar{k}_z\right\}\mathrm{e}^{-\mathrm{i}n\bar{\phi}}. \tag{44}$$

The integration contour of this solution is identical to that of the incident field [Eq. (33)].

III. VALIDATION

A. Implementation

Only brief details about the implementation procedure are mentioned in this article since similar details about the numerical implementation are given in the previous articles on this work by the authors.[10,11] The Wiener–Hopf solution for a spinning mode has been implemented directly into the installation acoustics code by adapting another in-house code named GXMUNT written by Gwénaël Gabard, based on the formulation derived by Gabard and Astley.[14]

The other difference between the new installation acoustics code, and the implementation described in Gaffney *et al.*,[11] is that all wavenumbers in the Wiener–Hopf solution are taken to be complex. This means that no special treatment is required for the critical layer in the Pridmore-Brown equation, owing to this feature of the Wiener–Hopf solution. Consequently, it is no longer necessary to implement a Frobenius solution to integrate the Pridmore-Brown equation across the critical layer described in Gaffney *et al.*[11] (Sec. III). When implementing the Wiener–Hopf method it is crucial to select an appropriate integration contour. The integration path must ensure that all the split functions are regular, in order to apply Cauchy's integral theorem. This also applies to the inverse Fourier transform in Eq. (33), where the contour is displaced from the real axis.

B. Comparison between disk source and spinning mode source

In order to verify the results from the new installation acoustics code, results are compared between the disk source and the spinning mode source. Hocter[17] compared the Wiener–Hopf solution for a spinning mode and an approximate result obtained by the Kirchhoff approximation. The latter is directly comparable to the disk source model without the screen utilised in previous work by the authors.[10,11] Hocter showed a representative sample of directivity patterns covering low- and high-order modes with a range of mode propagation angles. In all these examples, the principal lobe was very similar in both predictions, but all the directivity patterns were significantly different on approaching $\theta = 90°$. It is not possible to identify a single polar angle where the two solutions start to differ because Hocter showed that it varied for different modes, but commonly the solutions differ starting at polar angles between 60° and 70°. Since differences in the directivity between the Wiener–Hopf solution for a spinning mode and the disk source model depend on the parameters which define the spinning mode, a key benefit of using the Wiener–Hopf method is that it removes this uncertainty by using a solution which is valid at all polar angles.

Figure 3 shows examples of the predicted sound pressure level on the cylindrical fuselage at $\bar{\phi} = 0$ and $0 \leq \bar{z} \leq 2$. The pressure is calculated using the disk source or the spinning mode source for the incident field. There is very close agreement between the two alternative predictions in the range $1 \leq \bar{z} \leq 2$. Closer to the source plane, in the range $0 \leq \bar{z} \leq 1$, the predictions differ, with typically a difference in excess of 5 dB at $\bar{z} = 0$. These predictions can be used to estimate $\theta_{\max}$, which corresponds to the maximum polar angle (measured as shown in Fig. 1) at which there is good agreement between the fuselage pressure levels, predicted by either the disk source or the spinning mode source. For the same parameters used with Fig. 3, the values of $\theta_{\max}$ in Table I are calculated for a selection of values of $\bar{z}$, whereby the value of $\bar{z}$ specifies the axial location where the two alternative predictions (disk source and spinning mode)

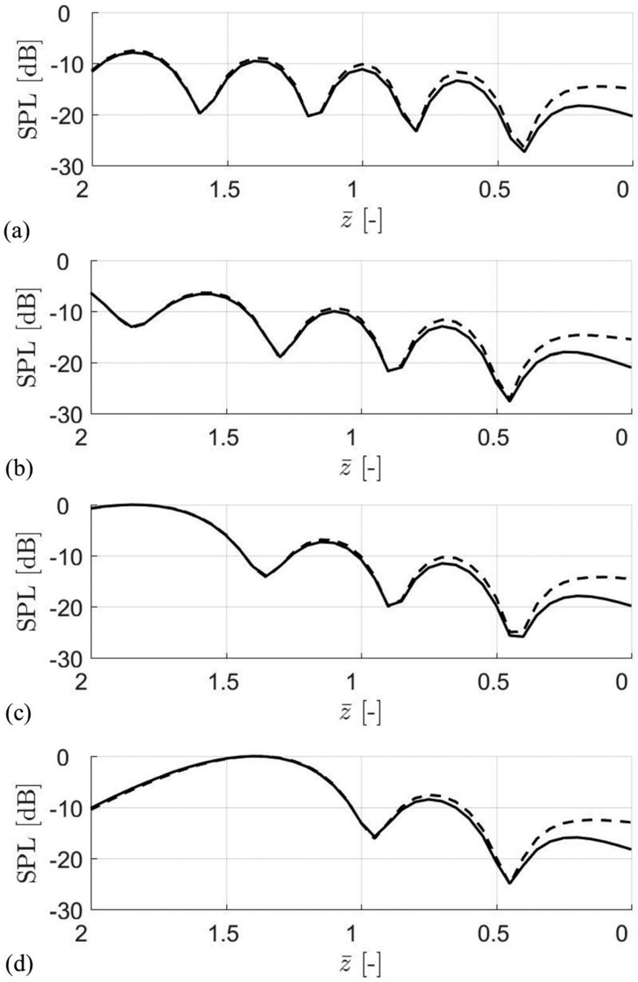

FIG. 3. Predictions of the normalised SPL at $\bar{\phi} = 0$ for the disk source and spinning mode source. The mean flow is uniform with no boundary layer. The relevant parameters are $k_0a = 20$, $a = 0.5$, $b = 3$, and $M_\infty = 0.75$. (a) $(l, q) = (4, 1)$, (b) $(l, q) = (11, 1)$, (c) $(l, q) = (14, 1)$, and (d) $(l, q) = (17, 1)$. Key: disk source (– –); spinning mode (—).

TABLE I. Estimates of $\theta_{\max}$ using the same parameters as in Fig. 3.

$\bar{z}$ []	0.5	1.0	1.5	2.0
$\theta_{\max}$	76°	63°	53°	45°

start to diverge. It is seen in Fig. 3 that the two predictions typically start to diverge in the range $0.5 \leq \bar{z} \leq 1$. This roughly corresponds to $\theta_{\max} \approx 70°$, which is similar to the findings in Hocter.[17]

Figure 4 shows the predicted sound pressure levels (SPL) on the whole cylindrical fuselage in the range $-5 \leq \bar{z} \leq 5$ for an incident field comprised of a single mode, calculated using either the disk source or the spinning mode source. This illustrates the region forward of the source plane where predictions using either of the incident fields give very similar levels. In contrast, closer to the source plane the predicted levels using the disk source are not realistic, because in the absence of a mean flow the disk source prediction would be symmetric about the source plane.

IV. ILLUSTRATIVE RESULTS

A. Boundary-layer shielding

This section focuses on the effect of boundary-layer refraction or shielding on a single mode radiated from an intake duct. The difference between the predicted sound pressure level with and without the boundary layer, at a point on the cylindrical fuselage, is defined by

$$\Delta\,[\mathrm{dB}] = \mathrm{SPL}_{bl} - \mathrm{SPL}. \tag{45}$$

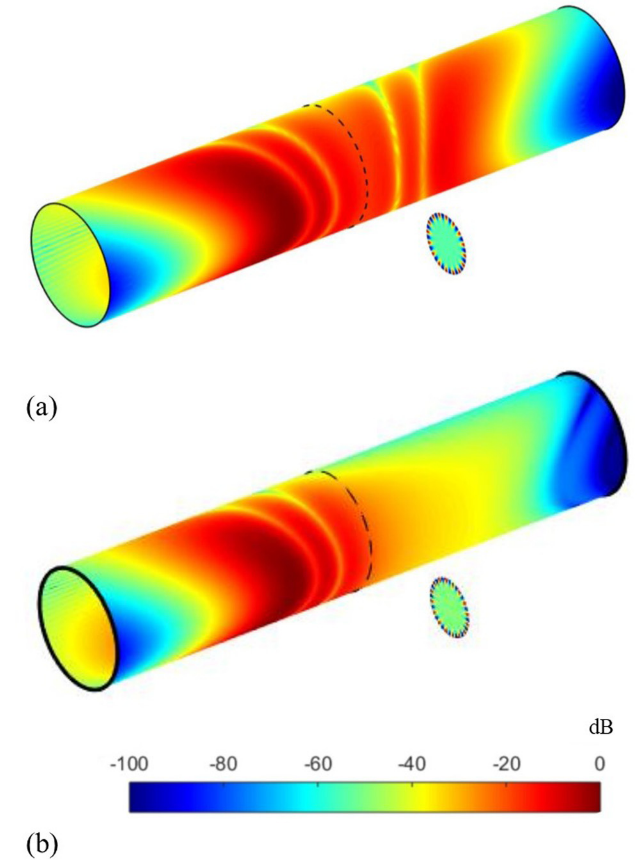

FIG. 4. (Color online) Normalised total SPL on the cylinder. Comparison between the disk source (a) and the spinning mode source (b). Note the dashed line marks the $\bar{z} = 0$ plane. The relevant parameters are $k_0 a = 20$, $a = 0.5$, $b = 3$, $(l, q) = (16, 1)$, and $M_\infty = 0.75$.

An example of Δ at $\bar{\phi} = 0$ and $-5 \leq \bar{z} \leq 5$ for a quarter-sine boundary layer is shown in Fig. 5. The Helmholtz number in these results is fixed at $k_0 a = 20$ (a realistic blade passing frequency), whilst the thickness of the boundary layer is varied from a very thin profile, $\delta = 0.0025$, to a thick profile, $\delta = 0.1$, as defined by 99% of the freestream velocity. For all the different boundary-layer thicknesses, there is little effect of boundary-layer refraction downstream of the source plane ($\bar{z} < 0$). However, upstream of the source ($\bar{z} > 0$), large reductions in the levels are predicted, caused by boundary-layer shielding as the upstream propagating sound is refracted away from the surface of the cylindrical fuselage. Even the very thin boundary-layer, $\delta = 0.0025$, is predicted to give a reduction of nearly 20 dB, compared to without the boundary layer, at $\bar{z} = 5$. This reduction in the predicted SPL increases as the thickness of the boundary layer is increased, and can lead to effectively total shielding with a thick boundary layer.

In order to quantify the effect of the boundary layer shielding over the whole cylinder, in Gaffney *et al.*[11] a simple shielding coefficient was introduced, defined by

$$S = \frac{(1/A)\int_A \overline{p^2}_{bl}\,\mathrm{d}A}{(1/A)\int_A \overline{p^2}\,\mathrm{d}A} \approx \frac{\sum^{\mathcal{M}} \overline{p^2}_{bl}}{\sum^{\mathcal{M}} \overline{p^2}}, \tag{46}$$

where in practice it is sufficient to evaluate S via a sum of the predicted mean square pressures over the $\mathcal{M}$ grid points distributed over the cylinder surface. The value of S will be between 0 and 1, where zero represents total shielding and unity represents no shielding.

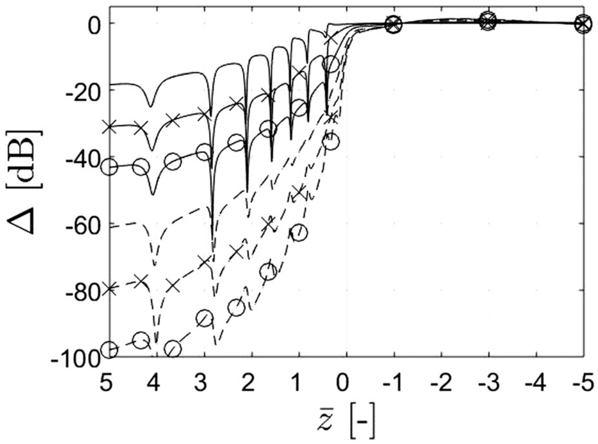

FIG. 5. Predictions of Δ at $\bar{\phi} = 0$ for the spinning mode source. The boundary-layer profile is quarter-sine with boundary-layer thickness δ varying from 0.0025 to 0.1. The other relevant parameters are $(l, q) = (4, 1)$, $k_0 a = 20$, $a = 0.5$, $b = 3$, and $M_\infty = 0.75$. Key: $\delta = 0.0025$ (solid line, no symbols), $\delta = 0.01$ (solid line, ×), $\delta = 0.025$ (solid line, ○), $\delta = 0.05$ (dashed line, no symbols), $\delta = 0.075$ (dashed line, ×), $\delta = 0.1$ (dashed line, ○).

However, in the previous work there were only simulation results upstream of the source plane. Therefore, in order to examine the effects of upstream and downstream sound propagation, additional shielding coefficients S_+ and S_- are defined

$$S_+ = \left.\frac{\sum^{\mathcal{M}_+}\overline{p^2}_{bl}}{\sum^{\mathcal{M}_+}\overline{p^2}}\right|_{\bar{z}>0} \quad \text{and} \quad S_- = \left.\frac{\sum^{\mathcal{M}_-}\overline{p^2}_{bl}}{\sum^{\mathcal{M}_-}\overline{p^2}}\right|_{\bar{z}<0}, \qquad (47)$$

where $\mathcal{M}_{+/-}$ denotes the grid points distributed over the cylinder's surface for $\bar{z} \gtrless 0$. It is emphasised that $S \neq S_+ + S_-$.

An illustrative result is shown in Fig. 6 with the same parameters used in the example shown in Fig. 5. In Fig. 6(a), the S_+ and S_- shielding coefficients are plotted against boundary-layer thickness from $\delta = 0$ to 0.1. This isolates the upstream and downstream effects of boundary-layer refraction. For upstream propagating sound only a relatively thin boundary layer is required for very significant shielding to be predicted. For downstream propagating sound some modest shielding is predicted, but in fact this is due to the difference in the predictions on the far side of the cylinder (not shown). In Fig. 6(b) the total shielding over the whole cylinder (upstream and downstream combined) is very significant, even for thin boundary layers, owing to the shielding of sound propagating upstream of the source plane.

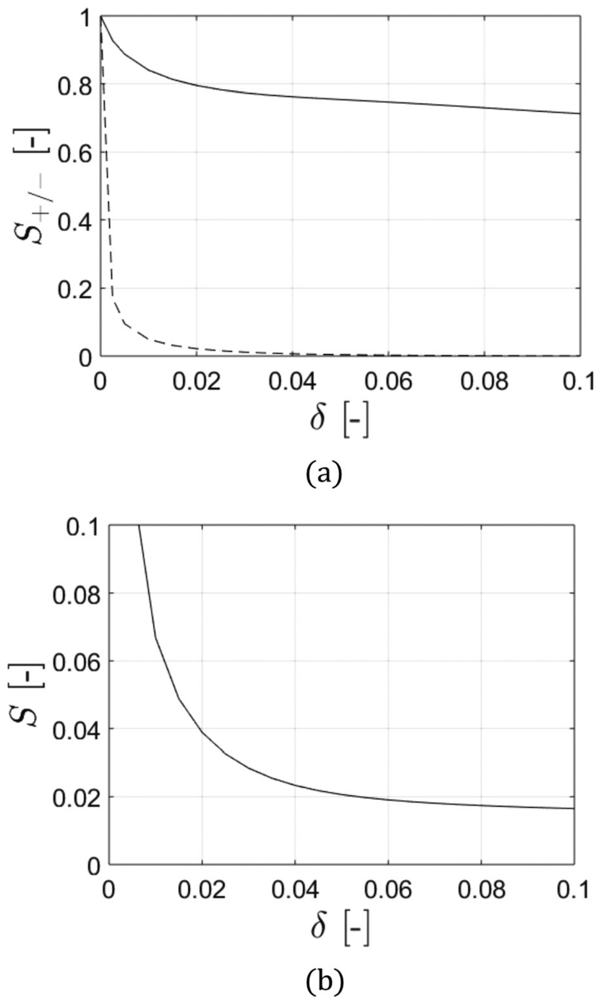

(a)

(b)

FIG. 6. Prediction of the shielding coefficient S for the quarter-sine boundary layer profile with varying boundary-layer thickness δ: (a) S_+ (dashed line) and S_- (solid line); (b) S. The relevant parameters are $(l, q) = (4, 1)$, $k_0 a = 20$, $a = 0.5$, $b = 3$, and $M_\infty = 0.75$.

B. Multi-mode simulations

In Gaffney *et al.*[11] the illustrated results showing the effect of boundary-layer shielding were for a single incident mode. However, a multi-mode source provides a better representation of fan tone radiation. This section presents some multi-mode results.

From Sec. II C, the surface pressure $\hat{p}_t$ [Eq. (44)] is expressed in terms of an inverse Fourier transform of the function $\tilde{\alpha}_n(k_z)$ [Eq. (41)], where $\tilde{\alpha}_n$ is the product of the functions $\tilde{\Lambda}_n(k_z)$ [Eq. (42)] and $\tilde{\eta}_n(k_z)$ [Eq. (43)]. The evaluation of $\tilde{\Lambda}_n$ is the principal time-consuming step in the method, since it involves the numerical integration of the Pridmore-Brown equation through the boundary layer. However, $\tilde{\Lambda}_n$ is independent of the incident mode order (l, q); only the function $\tilde{\eta}_n$ is dependent on (l, q). This means that multi-mode results can be calculated very efficiently, because for a fixed frequency the function $\tilde{\Lambda}_n(k_z)$ is only required to be evaluated once. For the simulation results shown in this section, an incoherent sum of all the cut-on modes is performed, but despite the incoherent sum involving 127 modes, the total run-time is only around twice the computation time that is required for a single mode.

The simulation results shown in Fig. 7 are for a multi-mode source with equal power per (cut-on) mode, whereas in Fig. 8 the results are for a multi-mode source with equal power per mode, except mode $(l, q) = (16, 1)$ which is 45 dB higher. This type of scenario reflects the situation where one or more modes may be dominant owing to the type of source mechanism, for example, rotor-locked modes which are dominant when the rotor-locked pressure field is cut on.

In both examples, the total SPL on the surface of the cylinder is shown for the range $-5 \leq \bar{z} \leq 5$. At $\bar{z} = 5$, with the thin boundary-layer the predicted SPL is approximately 20 dB less than is predicted with uniform flow (no boundary layer). With the thick boundary-layer the predicted SPL is approximately 50 dB less compared with no boundary layer. These reductions are due to the boundary-layer refracting the sound away from the cylinder, and, as expected, the effect of boundary-layer shielding is much more significant with the thick boundary layer.

Contrastingly, downstream of the source plane the predicted levels with uniform flow or the thin boundary layer are very similar. There are small differences compared with the thick boundary-layer, but, also as expected, the effect of boundary-layer shielding is rather small, since the downstream propagating sound is refracted towards the cylinder. This effect causes the slight increase in amplitude downstream of the source.

Finally, in Fig. 8 the directivity pattern of mode $(l, q) = (16, 1)$ is visible, mapped onto the surface of the cylinder. The intersection of the principal lobe corresponds to the area of highest SPL. Overall, the results in Fig. 8 are very similar to the results in Fig. 7, but with the effective directivity

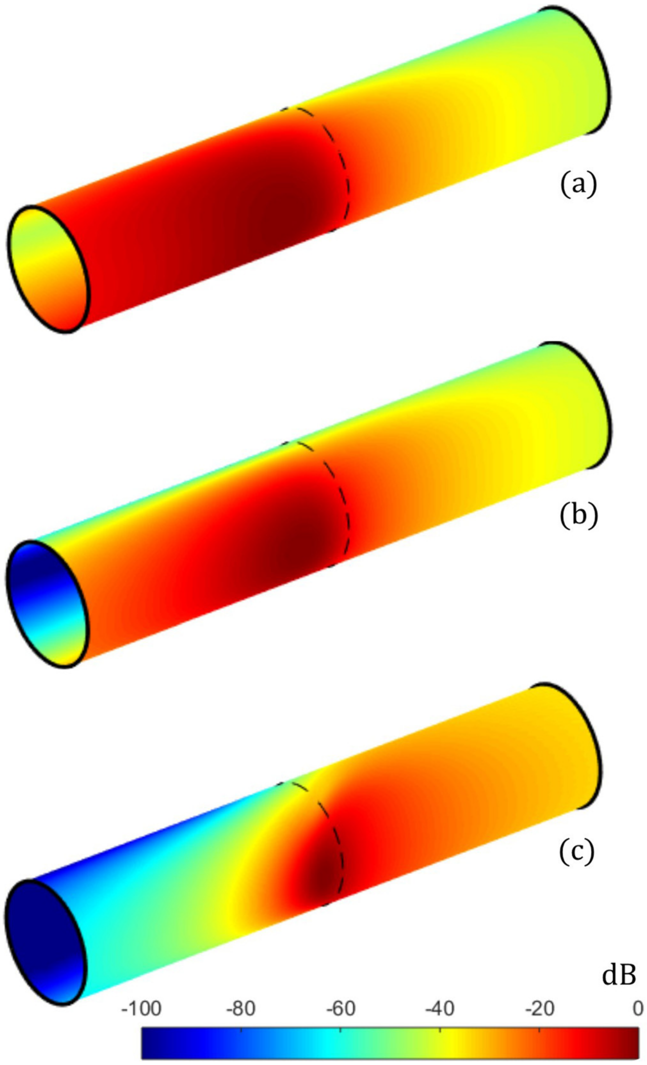

FIG. 7. (Color online) Normalised total SPL on the surface of the cylinder for an incoherent, multi-mode source with equal power per mode: (a) uniform flow, $\delta = 0.0$; (b) $\delta = 0.01$; and (c) $\delta = 0.1$. The boundary-layer profile is quarter-sine. The dashed line shows the position of the source plane $\bar{z} = 0$ (the source is not shown). The relevant parameters are $k_0 a = 20$, $a = 0.5$, $b = 3$, and $M_\infty = 0.75$.

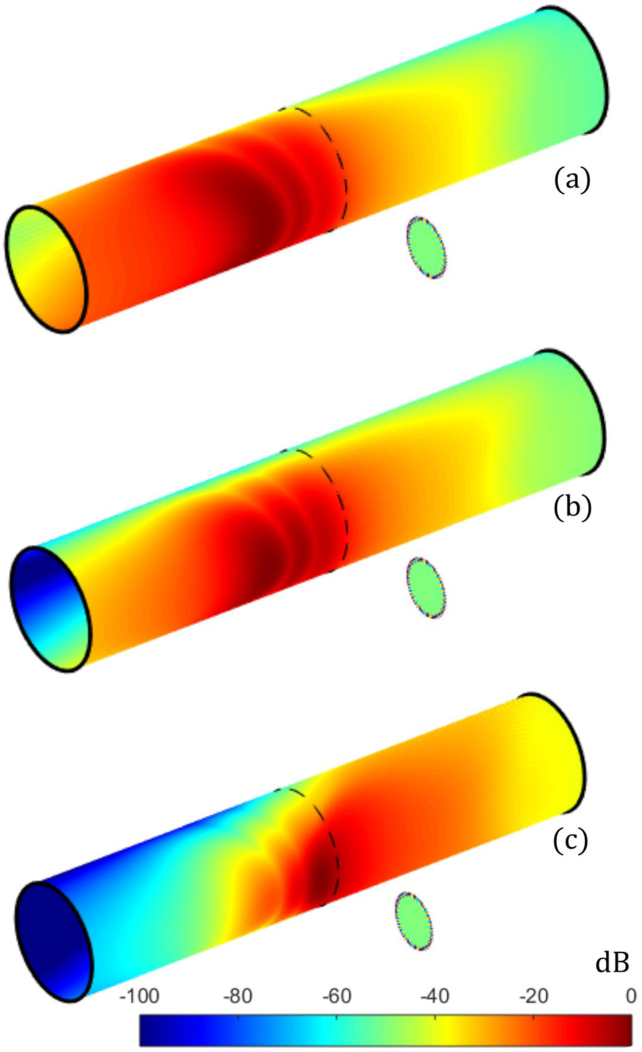

FIG. 8. (Color online) Normalised total SPL on the surface of the cylinder for an incoherent, multi-mode source with equal power per mode except $(l, q) = (16, 1)$ whose modal amplitude is set 45 dB higher: (a) uniform flow, $\delta = 0.0$; (b) $\delta = 0.01$; and (c) $\delta = 0.1$. The boundary-layer profile is quarter-sine. The dashed line shows the position of the source plane $\bar{z} = 0$. The relevant parameters are $k_0 a = 20$, $a = 0.5$, $b = 3$, and $M_\infty = 0.75$.

pattern of the protruding mode imposed on the visualisations of the total sound pressure levels.

V. DISCUSSION

Nayfeh *et al.*[18] showed that inside a flow duct, predictions quantifying the effect of boundary-layer shielding showed similar results for different boundary-layer profiles if the different profiles were scaled such that they had the same displacement thickness ($\delta^\star$). The exception was the power-law profile which is commonly used to model a turbulent boundary layer.

A similar illustrative example is shown in Fig. 9, based on the exterior problem considered in the present work, i.e., boundary-layer shielding on the external surface of a cylindrical fuselage. Predictions of Δ [Eq. (45)] for three boundary-layer profiles are compared. The profiles are linear, quarter-sine and 1/7th power law with linear sublayer of thickness 0.001 δ. The results show predictions of Δ versus $\delta^\star$ at two different locations on the fuselage. The range of $\delta^\star$ from zero to 0.0125 is equivalent to varying the boundary-layer thickness δ from zero to 0.1 for the 1/7th power-law profile. In Fig. 9 it is seen that at both locations on the cylinder, the predictions of Δ obtained with the linear or quarter-sine profiles are almost identical, but the predictions with the power-law profile differ from the other two profiles. This is consistent with the previous findings reported by Nayfeh *et al.* for the flow duct problem.

Also in Fig. 9, the results clearly show that for thin boundary layers the rate-of-change of Δ is nonlinear as $\delta^\star$ is increased, whereas for thicker boundary layers the change in Δ is linearly proportional to the change in $\delta^\star$.

It is possible to predict similar values of Δ obtained with the power-law profile by utilising a simple, discontinuous, "step velocity" profile. The step velocity profile is taken to be zero for $1 < \bar{r} < 1 + \tau\delta$, and equal to M_∞ for $1 + \tau\delta < \bar{r}$, where δ is the thickness of the power-law boundary layer. There is a discontinuous step change in the velocity from zero to the free-stream value at $\bar{r} = 1 + \tau\delta$. Predictions of

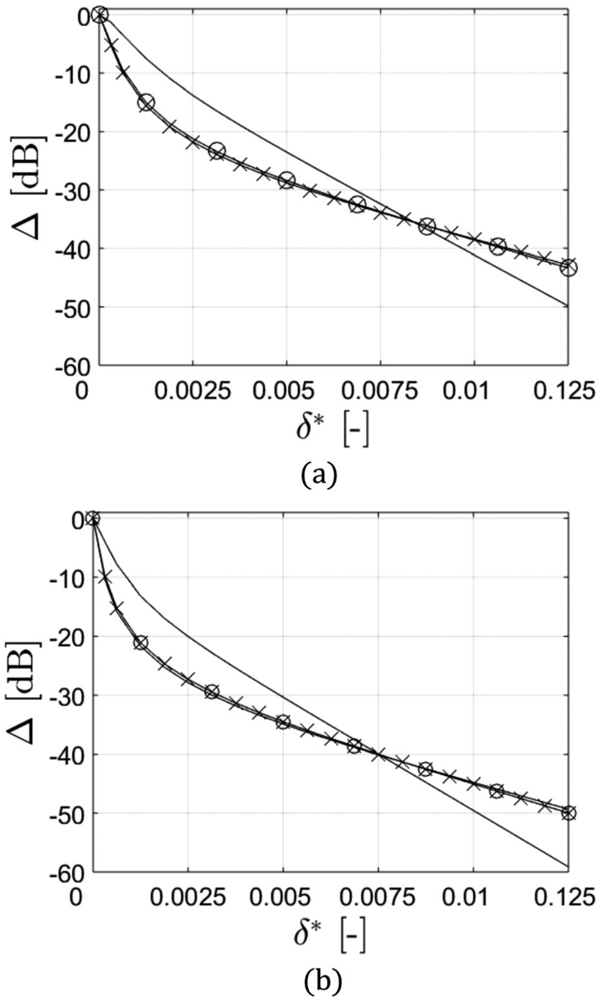

(a)

(b)

FIG. 9. Predictions of Δ versus boundary-layer displacement thickness $\delta^{\star}$ for three different velocity profiles. The 1/7th power-law boundary layer is compared against linear and quarter-sine boundary-layer profiles at (a) $\bar{\phi} = 0$, $\bar{z} = 0$ and (b) $\bar{\phi} = 0$, $\bar{z} = 5$. The relevant parameters are $(l, q) = (4, 1)$, $k_0 a = 20$, $a = 0.5$, $b = 3$, and $M_\infty = 0.75$. Key: power-law (solid line); linear (solid, ×); quarter-sine (solid, ○).

Δ versus δ for the 1/7th power-law boundary-layer profile, and the step velocity profile with $\tau = \frac{1}{3}$, are shown in Fig. 10. Results are compared at locations upstream ($\bar{z} = 5$), downstream ($\bar{z} = -5$), and in the source plane ($\bar{z} = 0$). There is excellent agreement between the two separate predictions of Δ upstream of the source, where shielding will be very significant. Thus, it is seen that the step velocity profile (with an appropriate value of τ) could be used instead of the power-law profile to calculate realistic predictions of boundary-layer shielding. The benefit of this approach is that a fully analytical solution can be derived for a step velocity profile because there is no sheared flow. Consequently, the calculations are extremely quick, comparable with the calculations for uniform flow with no fuselage boundary layer.

VI. CONCLUSIONS

In this article, the key advancement to a theoretical model for calculating the fuselage pressure levels due to fan tones radiated from the intake of an installed turbofan aero-engine is the use of a Wiener–Hopf solution of a spinning mode exiting a cylindrical duct to specify the incident field. As in previous work by the authors,[10,11] the total field is given by the sum of the incident and scattered fields, and is calculated with the inclusion of refraction by the fuselage boundary layer. The advanced method enables more representative predictions to be obtained in the region around the source plane, up to a maximum polar angle $\theta_{\max} > 90°$, after which point the intake fan noise ceases to the dominant source of noise incident on the fuselage.

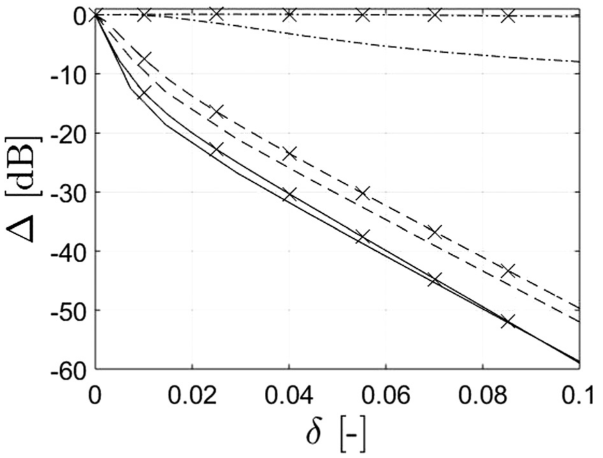

FIG. 10. Predictions of Δ versus boundary-layer thickness δ for two different velocity profiles. The 1/7th power-law boundary layer is compared against the step-change profile, with step thickness equal to one-third of the boundary-layer thickness. Results are shown at $\bar{\phi} = 0$ and $\bar{z} = 5$, 0, and −5. The relevant parameters are $(l, q) = (4, 1)$, $k_0 a = 20$, $a = 0.5$, $b = 3$, and $M_\infty = 0.75$. Key: $\bar{z} = 5$ (solid lines), $\bar{z} = 0$ (dashed lines), $\bar{z} = -5$ (dashed-dot lines), power-law (crosses), and step-change (no symbol).

This work focuses on the prediction of intake fan tones, such as "buzz-saw" tones, and the incident sound on the fuselage forward of the wings. However, the radiation of bypass fan tones also is applicable using the Wiener–Hopf technique, and has been examined by a number of authors including Munt,[16] Rienstra,[19] Gabard and Astley,[14] Samanta and Freund,[20] and Veitch and Peake.[21] Thus there is scope to use the Wiener–Hopf method to construct the incident field for a fan tone radiated from the bypass duct, and to incorporate this into the installation acoustics method. However, this problem has significant added complexity, compared to the intake noise radiation problem. Other tonal sources, such as turbine tones, are radiated from the engine's exhaust. Sound radiated from the exhaust propagates through the jet shear layers which causes refraction, and also, potentially, spectral broadening or "haystacking" of tonal sound fields. Additionally, for the installation acoustics problem, exhaust noise radiation will be affected by the wings for wing-mounted engines. Thus, for incident sound on the fuselage downstream of the wings, there are number of additional issues that would need to be examined. Recently, the current focus of research in this area has focussed on the issue of jet-wing interaction, which could be a more significant source of the aft noise radiation.

Illustrative results show that boundary-layer shielding forward of the source can be very significant. It is also highlighted that it is possible to obtain realistic estimates of the shielding without necessarily modelling the realistic boundary-layer profile. It may be sufficient to ensure that the profile has realistic thickness parameters, without necessarily having to determine the realistic mean-flow profile.

It is also shown that multi-mode sources can be simulated very efficiently using this approach, without any prohibitive increase in the computational cost compared to simulations for a single mode.

In summary, the fidelity of this theoretical model for installation acoustics is comparable with previous methods which had been developed for propeller noise sources, but not for turbofan noise sources. The incident field can be calculated using the Wiener–Hopf solution which is valid at all polar angles, thus predictions can be extended downstream as well as upstream of the source plane. However, it is emphasised that further downstream the fuselage pressure levels will be dominated by exhaust noise sources.

All the data supporting this study is openly available from the University of Southampton Repository.[22]

ACKNOWLEDGMENTS

The authors wish to thank Gwénaël Gabard who kindly provided the Wiener–Hopf code GXMUNT for use in this work, and for informative discussions on the theory that he had developed in a previous article (Gabard and Astley[14]). Also, the authors wish to acknowledge the continuing financial support provided by Rolls-Royce plc through the University Technology Centre in Gas Turbine Noise at the Institute of Sound and Vibration Research. J.G. also acknowledges the financial contribution from the EPSRC via the University of Southampton's DTP grant.

[1] J. Bowman, T. Senior, and P. Uslenghi, *Electromagnetic and Acoustic Scattering by Simple Shapes* (North-Holland, Amsterdam, 1969).

[2] G. McAninch, "A note on propagation through a realistic boundary layer," J. Sound Vib. **88**, 271–274 (1983).

[3] D. Hanson, "Shielding of prop-fan cabin noise by the fuselage boundary layer," J. Sound Vib. **92**, 591–598 (1984).

[4] D. Hanson and B. Magliozzi, "Propagation of propeller tone noise through a fuselage boundary layer," J. Aircraft **22**, 63–70 (1985).

[5] H. Lu, "Fuselage boundary-layer effects on sound propagation and scattering," Am. Inst. Aeronaut. Astron. J. **28**, 1180–1186 (1990).

[6] I. Belyaev, "The effect of an aircraft's boundary layer on propeller noise," Acoust. Phys. **58**, 425–433 (2012).

[7] H. Brouwer, "The scattering of open rotor tones by a cylindrical fuselage and its boundary layer," in *Proceedings of the 22nd AIAA/CEAS Aeroacoustics Conference*, Lyon, France, AIAA Paper No. 2016-2741 (30 May–1 June, 2016).

[8] M. Siefert and J. Delfs, "Refraction and scattering in high Mach number boundary layers," in *Proceedings of the 17th AIAA/CEAS Aeroacoustics Conference*, AIAA 2011-2847, Portland, Oregon (June 5–8, 2011).

[9] J. Dierke, R. Ewert, J. Delfs, C. Stoehr, and M. Rose, "The effect of a boundary layer on engine noise propagating to the fuselage at flight conditions," in *Proceedings of the 19th AIAA/CEAS Aeroacoustics Conference*, AIAA 2013-2006, Berlin, Germany (May 27–29, 2013).

[10] A. McAlpine, J. Gaffney, and M. Kingan, "Near-field sound radiation of fan tones from an installed turbofan aero-engine," J. Acoust. Soc. Am. **138**, 131–1324 (2015).

[11] J. Gaffney, A. McAlpine, and M. Kingan, "Fuselage boundary-layer refraction of fan tones radiated from an installed turbofan aero-engine," J. Acoust. Soc. Am. **141**, 1653–1663 (2017).

[12] J. Tyler and T. Sofrin, "Axial flow compressor noise studies," SAE Trans. **70**, 309–332 (1962).

[13] G. Homicz and J. Lordi, "A note on the radiative directivity patterns of duct acoustic modes," J. Sound Vib. **41**, 283–290 (1975).

[14] G. Gabard and R. Astley, "Theoretical model for sound radiation from annular jet pipes: Far- and near-field solutions," J. Fluid Mech. **549**, 315–341 (2006).

[15] Gabard and Astley define time-harmonic waves using the convention $\exp\{-\mathrm{i}\,\omega_0\,t\}$ and take the duct radius a as the reference lengthscale. In the current article, the convention used for time-harmonic waves is $\exp\{\mathrm{i}\,\omega_0\,t\}$ and the reference lengthscale is the cylinder radius a_0.

[16] R. Munt, "The interaction of sound with a subsonic jet issuing from a semi-infinite cylindrical pipe," J. Fluid Mech. **83**, 609–640 (1977).

[17] S. Hocter, "Exact and approximate directivity patterns of the sound radiated from a cylindrical duct," J. Sound Vib. **227**, 397–407 (1999).

[18] A. Nayfeh, J. Kaiser, and B. Shaker, "Effect of mean-velocity profile shapes on sound transmission through two-dimensional ducts," J. Sound Vib. **34**, 413–423 (1974).

[19] S. W. Rienstra, "Acoustic radiation from a semi-infinite annular duct in a uniform subsonic mean flow," J. Sound Vib. **94**, 267–288 (1984).

[20] A. Samanta and J. Freund, "Finite-wavelength scattering of incident vorticity and acoustic waves at a shrouded-jet exit," J. Fluid Mech. **612**, 407–438 (2008).

[21] B. Veitch and N. Peake, "Acoustic propagation and scattering in the exhaust flow from coaxial cylinders," J. Fluid Mech. **613**, 275–307 (2008).

[22] University of Southampton Repository, https://doi.org/10.5258/SOTON/D0533 (Last viewed 25 May 2018).